





Article

Unravelling the Chemistry of the [Cu(4,7-Dichloroquinoline)₂Br₂]₂ Dimeric Complex through Structural Analysis: A Borderline Ligand Field Case

Giada Finocchio ¹, Silvia Rizzato ¹, Giovanni Macetti ², Gers Tusha ¹
and Leonardo Lo Presti ^{1,*}

¹ Department of Chemistry, Università degli Studi di Milano, Via Golgi 19, 20133 Milano, Italy; giadafinocchio@libero.it (G.F.); silvia.rizzato@unimi.it (S.R.); gerstusha@gmail.com (G.T.)

² Laboratoire de Physique et Chimie Théoriques, Université de Lorraine and CNRS, 1 Boulevard Arago, F-57078 Metz, France; giovanni.macetti@univ-lorraine.fr

* Correspondence: leonardo.lopresti@unimi.it

Received: 18 May 2020; Accepted: 30 May 2020; Published: 4 June 2020



Abstract: Large dark prismatic crystals ($P\bar{1}$) consisting of closely packed centrosymmetric [Cu(4,7-dichloroquinoline)₂Br₄] binuclear units are formed when 4,7-dichloroquinoline (DCQ, C₉H₅NCl₂) binds copper(II). Cu²⁺ adopts a strongly distorted square pyramidal coordination geometry, perturbed by electrostatic interactions with two axial μ -Br ligands acting as highly asymmetric bridges. It is shown that, as electronic states of ligands are higher in energy than the metal ones, antibonding orbitals bear significant ligand-like character and electronic charge is partially transferred from inner-sphere coordinated halogen atoms to copper. Overall, the title compound sits on the Hoffman's border between main group and transition chemistry, with non-negligible contributions of the ligands to the frontier orbitals. The relative energy placement of metal and ligand states determines an internal redox process, where the metal is slightly reduced at the expense of partial oxidation of the bromide ligands. In fact, the crystal structure is partially disordered due to the substitution of some penta-coordinated Cu(II) centers with tetra-coordinated Cu(I) ions. The geometry of the complex is rationalized in terms of electrostatic-driven distortions from an ideal octahedral prototype. Implications on the reactivity of Cu(II)-quinoline complexes are discussed.

Keywords: copper; inverted ligand field; ligand field theory; experimental charge density; quantum theory of atoms in molecules; 4,7-dichloroquinoline

1. Introduction

Because of its versatility, Cu²⁺ has been defined as a chameleon in coordination chemistry [1]. The stereochemistry of copper complexes is frequently dominated by a subtle interplay of Jahn–Teller, dynamic and steric effects [2,3] that cause it to depart from that expected based on a simple crystal field framework [4]. The discovery of an inverted ligand field in Cu-based coordination compounds [5–7], prototyped by the square planar anion Cu(CF₃)₄[−], deepened the general understanding of coordinative bonding [8] and provided new ways to exploit the reactivity of unusual chemical states of both the metal and the ligands. In a recent review [8], Hoffmann and co-workers pointed out that late transition elements like Cu and Zn lie on the borderline of what they define as “transition metal thinking” and “main group thinking”. In other words, the metal itself might present a sort of σ -noninnocence, that is, its 3d states could be as much important as the 4s-4p ones in determining the measured geometrical

and electronic properties of the complex. This kind of analysis definitely suggests the existence of a very rich territory of yet unexplored chemistry.

For some years now, we have been studying the reactivity of transition metals with quinoline-based antimalarial drugs in order to understand their mechanism of action at the molecular level [9–11]. Quinoline compounds can actively enter the metabolism by binding specific metal targets, including late transition elements like copper and zinc [12]. Iodochlorhydroxyquin (clioquinol) [13] and 7-chloroaminoquinolines [14], for example, are effective Cu(II) scavengers, with potential application against Alzheimer’s disease [13–15]. Chloroquine and hydroxychloroquine were recently claimed to even exploit antiviral activity against pandemic SARS-CoV2 virions, even though the exact mechanism of action remains to be elucidated [16]. Cu:quinoline complexes can also promote the decarboxylation of aromatic acids, as cuprous ions stabilize anionic transition states by setting up π bonds with the occupied p-like orbitals of the substrate [17,18]. Due to manifest implications on general reactivity and medicinal applications, a deeper understanding of chemical bonding in copper:quinoline complexes is desirable. Moreover, these systems are good candidates for probing chemical and structural properties on the edge of Hoffmann’s traced boundary.

Here, a newly synthesized binuclear Cu(II) coordination compound with 4,7-dichloroquinoline (4,7-DCQ, $C_9H_5NCl_2$, Figure 1) and bromide ligands is discussed (hereinafter, CDCQB). To date, only the structures of trichloroacetate and benzoate Cu(II) copper complexes with 4,7-DCQ are known [19], even though a similar binuclear core structure was reported in quinoline:Cu(I) complexes with Cl, Br and I as μ^2 -bridging ligands [20,21]. The main goal is to clarify how chemical bonding in the title compound is related to the metal valence state, from which the observed coordination geometry stems. CDCQB was probed by single-crystal X-ray diffraction experiment at $T = 100$ K and magnetic measurements. Experimental results were complemented by quantum simulations at the DFT M06 level, while the real-space analysis of the experimental electron density, carried out in the framework of the quantum theory of atoms in molecules [22], was exploited to translate the Hilbert space picture into a more familiar chemical lexicon.

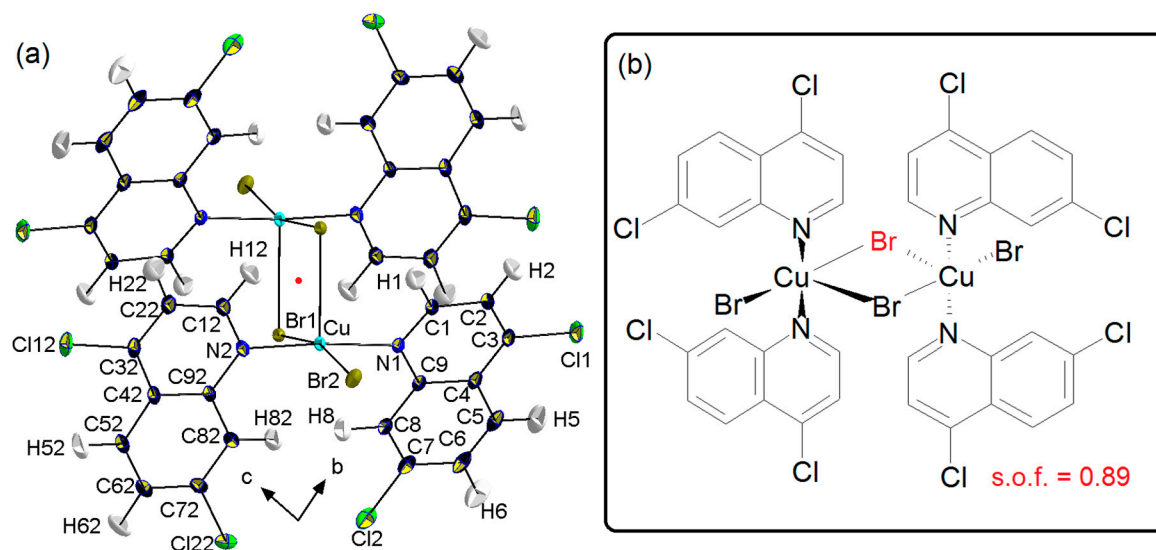


Figure 1. (a): Single-crystal X-ray structure of the centrosymmetric CDCQB complex at 100 K, with the atom numbering scheme, as viewed down the a axis. The center of symmetry (red dot) coincides with the center of coordinates. Thermal ellipsoids are drawn at the 50% probability level. Anisotropic displacement parameters were assigned to hydrogen atoms according to the procedure implemented in the Shade [23] server. (b): Chemical connectivity of CDCQB. The Br atom drawn in red corresponds to Br(1) and is occupationally disordered with site occupation factor (s.o.f.) of 0.89 (see Section 2).

2. Methods

2.1. Synthesis

Reagent-grade chemicals were purchased from Aldrich and used without further purification. A ~120 mM transparent solution was prepared by dissolving under stirring 47.2 mg of DCQ into 2.0 mL of CH₂Cl₂ and then poured in a glass test tube (Ø 9 mm). A ~60 mM yellow solution of CuBr₂ was also prepared by dissolving 26.9 mg of CuBr₂ into 2.0 mL of methanol under stirring. Then, the copper solution was layered gently over the DCQ solution with a Pasteur pipette. The test tube was sealed with Parafilm and was allowed to rest at ambient temperature for roughly 76 h. After ~24 h, the mixture became homogeneously pale yellow-colored. In the next two days, a number of yellow, tiny acicular crystals appeared in the bulk liquor. Their quality was generally low; preliminary single-crystal X-ray diffraction analysis showed that they consisted of a copper-containing *P2₁/c* monoclinic phase, which will be described in detail in a forthcoming study on the reactivity of such complexes. After 5 days, the test tube was put in a refrigerator at *T* = 6–8 °C, where it rested for roughly a month. Thirteen days after the preparation, the first tiny black crystal appeared in the liquor; in the next days, the crystals of the new phase grew in number and dimensions, coexisting with the pristine yellow ones. The crystallization was deemed concluded roughly 30 days after the preparation. Upon extensive testing, a charge-density quality specimen of the black phase (Figure S1) was selected for the diffraction analysis.

2.2. Single-Crystal X-ray Diffraction and Model Refinement

Diffraction experiments at 100 K were carried out on a Bruker AXS Smart Apex three-circle diffractometer equipped with an Apex II CCD area detector and an Oxford Cryosystem N₂ blower. Graphite-monochromated X-rays at the characteristic Mo K α wavelength (λ = 0.71073 Å) were produced with a sealed tube at a nominal 50 kV \times 30 mA power of the generator. Diffraction data were acquired in ω -scan mode up to a maximum resolution of 0.44 Å. No phase transitions were detected in the RT to 100 K range. The data were integrated with SAINT+, while frame scale factors and an empirical absorption correction were applied with SADABS [24]. Attempts to develop analytical absorption correction models were unsatisfactory, as the deep black color of the specimen made very difficult to accurately reconstruct the boundaries of the crystal faces. The empirical absorption procedure nevertheless gave satisfactory results for our regularly shaped specimen. It consists in fitting a multipole-based transmission surface against expected average intensities of multiple measures of equivalent intense reflections and determining an overall internal agreement factor of 2.6% up to $\sin\theta/\lambda$ = 1.0 Å⁻¹ (Table 1). Moreover, statistical analysis (see Figure S4) demonstrated that no significant residual systematic errors were present in the reduced dataset. The structure was solved by direct methods and refined in the spherical atom formalism framework implemented in the SHELX suite of programs [25]. A bromide ion in the first coordination shell of one of the two Cu atoms was found to be occupationally disordered, with the site occupation factor refining to 0.8870(6). Table 1 summarizes the most relevant crystallographic results. CCDC 2002857 contains the supplementary crystallographic data for this paper. These data can be obtained free of charge from The Cambridge Crystallographic Data Centre via www.ccdc.cam.ac.uk/structures.

2.3. Magnetic Measurements

The molar magnetic susceptibility of the powdered material was measured with an Alfa Aesar magnetic susceptibility balance Mark 1 at *T* = 291 K. Diamagnetic corrections due to atoms, ions and chemical bonds in CDCQB were calculated from tabulated Pascal constants [26].

2.4. Quantum Simulations (Gas Phase)

The structure of the title compound was optimized in vacuo with Gaussian09 [27], starting from the X-ray geometry. The Minnesota-class meta-GGA M06 DFT functional [28] was exploited to account

for long-range dispersion effects [29], in conjunction with the triple zeta valence polarization (TZVP) basis set proposed by Peintinger [30]. A restricted basis was employed, considering both the singlet and triplet spin states of the complex. As the ground state charge density does not depend on the spin state, only the singlet results are considered in the discussion of chemical bonding, unless otherwise specified. Vibrational frequencies were calculated to confirm that the optimized structures correspond to true potential energy minima. Energy differences always account for zero-point vibrational corrections.

Table 1. Data collection statistics and relevant refinement details of CDCQB ^a at T = 100 K.

Crystal Data		
a (Å)	7.8673(5)	
b (Å)	11.0031(7)	
c (Å)	11.7131(6)	
α (deg)	82.325(2)	
β (deg)	89.994(2)	
γ (deg)	81.179(2)	
V (Å ³)	992.76(10)	
Density (g·cm ⁻³)	2.041	
Crystal size (mm)	0.350 × 0.225 × 0.200	
Data collection		
Measured/Unique refls.	81,711/16,169	
Observed refls. (I > 2σ(I))	13,645	
(sinθ/λ) _{max} /Å ⁻¹	1.00	
Completeness	0.973	
R _{int}	0.0264	
Refinement details	IAM model ^b	Multipole Refinement ^c
R(F)/wR(F ²)/goodness-of-fit ^d	0.0339/0.0670/1.061	0.0239/0.0333/1.011
Δρ _{max} /Δρ _{min} (e·Å ⁻³)	+1.356/−0.913	+0.497/−0.418
Spherical (ζ = κα) and deformation (ζ' = κ'α') atomic exponents ^e	//	Cu: κ = 1.004(1), κ' = 1.01(1) Br: κ = 1.052(2), κ' = 1.12(2) Cl: κ = 1.020(1), κ' = 0.99(2) N: κ = 1.004(1), κ' = 0.90(2) C: κ = 1.013(1), κ' = 0.952(4) H: κ = 1.230(6), κ' = 1.13(1)

^a Space group: P $\bar{1}$; molecular formula: C₃₆H₂₀Br₄Cl₈Cu₂N₄ (formal), C₃₆H₂₀Br_{3.77}Cl₈Cu₂N₄ (real); molecular weight: 1220.80 g·mol⁻¹; μ = 5.44 mm⁻¹; F₀₀₀ = 590 e. ^b Spherical atom model, with disorder included. ^c Anharmonicity and anisotropic charge density deformation included. A total of 15,521 independent data points have been included in the dataset after the exclusion of 644 unobserved reflections (F(hkl)² < 0) and 4 outliers. Full details can be found in the Supplementary Materials, Section S1. ^d All reflections. ^e Where not reported, least-squares estimated standard deviations are smaller than the last digit. Values in bohr⁻¹.

2.5. Experimental Charge Density Analysis

The deposited X-ray geometry at 100 K was corrected a posteriori by lengthening all the covalent C–H bond distances to their best neutron estimates [31]. Then, anisotropic displacement parameters (ADPs) of hydrogen atoms were evaluated with the TLS+U procedure [32], as implemented in the SHADE2.1 web server [23]. The site occupation factor of the disordered bromide ion was kept identical to that estimated based on the independent atom model (see above). The aspherical Hansen–Coppens rigid pseudoatom formalism [33] available in the XD2016 program suite [34] was exploited to fit all the symmetry-independent observed intensities (|F_{hkl}|² > 0) up to sinθ/λ = 1.00 Å⁻¹. The Su and Coppens [35] radial functions for core and valence densities of neutral atoms were taken from the embedded SCM databank and used throughout. The complexity of the least-squares model was incremented progressively, until quadrupoles (l = 2) for H; octupoles (l = 3) for C and N; and hexadecapoles (l = 4) for heavier Cl, Br and Cu atoms were included. Third-order Gram–Charlier coefficients were used for chlorine and bromine atoms to account for residual anharmonicity at low

temperature [36,37]. Radial scaling parameters κ and κ' for each atomic species were also refined. The experimental multipole model was compared with a theoretical one, obtained by projecting the same multipole expansion onto a set of synthetic structure factor amplitudes, F_{theo} , predicted from DFT single-point calculations of the CDCQB structure (see Section S1.4 of the Supplementary Materials). The interested reader can find full details in the Supplementary Materials (Section S1). Experimental and theoretical structure factor amplitudes, as well as input XD files, were also deposited. Relevant agreement factors are reported in Table 1.

3. Results

Crystal Packing

The CDCQB crystal is made by centrosymmetric neutral building blocks, each formed by two inversion-related asymmetric units. Only weak C–H hydrogen bond donors are present, not able to form strong extended networks. Thus, only dispersive interactions and high-order electrostatic moments are expected to determine the crystal packing [38]. The structure consists indeed of weakly bonded, isolated metal–organic units, the main inertial axis of the aromatic rings being oriented roughly along the $[10]$ direction (Figure 2a).

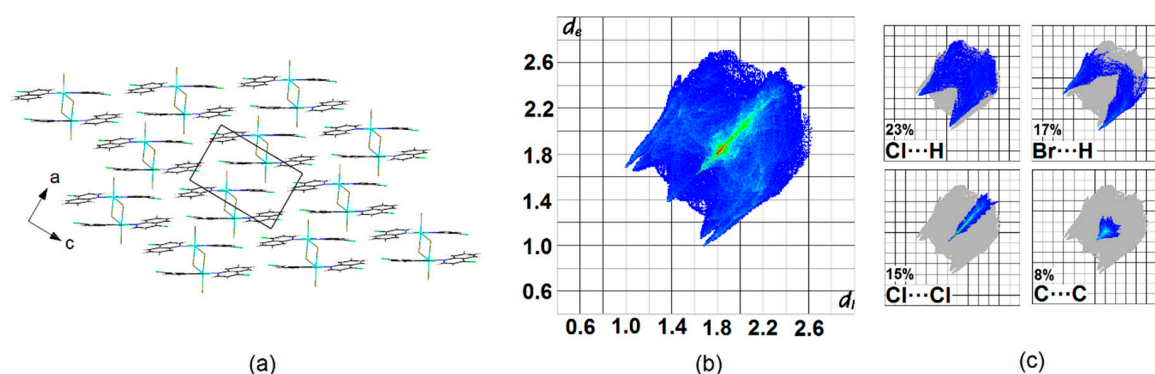


Figure 2. (a) Crystal packing of $[\text{Cu}(4,7\text{-DCQ})_2]_2\text{Br}_4$ at 100 K, as viewed down the b cell axis. The crystallographic unit cell is also shown. Atom color code is the same as Figure 1. (b) Hirshfeld surface fingerprint plot for the molecular unit (2 ASUs) at 100 K. (c) Specific atom–atom interactions are highlighted, and their percent surface coverage is displayed. Warmer colors correspond to higher contact frequencies; distances d_i (atom–surface, internal) and d_e (atom–surface, external) are in Å.

Figure 2b,c shows the Hirshfeld surface fingerprint plot of CDCQB in its crystalline environment at 100 K. As quinoline nitrogen atoms are directly involved in coordinative bonds with copper, the only available H-bond acceptors are Cl and Br species. The two spikes at $d_i + d_e \approx 2.7\text{--}2.9$ Å fingerprint close contacts of aromatic CH with halogens, together accounting for ~40% of the total surface of the plot. More information is available in Section S2 of the Supplementary Materials.

Other statistically relevant contacts are the Cl...Cl ones, which appear as a sharp plume along the main diagonal of the diagram. They correspond to weak type I halogen bonds [39] involving atoms Cl1 and Cl12 of neighboring 4,7-dichloroquinoline ligands, which form infinite chains running approximately along the $[1\bar{1}1]$ direction (Figure S7) and connected to each other through type II Cl2...Cl12 contacts (Figure S8). As expected, direct Br...Br interactions are missing, as negatively charged Br[−] ions tend to be as far apart as possible from each other [10,29]. As they are included in the first coordination sphere of Cu atoms, Br[−] ions are also unavailable to set up Br...Cl contacts.

The last significant feature appreciable from Figure 2 is a large blue leaf at $d_i + d_e \approx 3.8$ Å, roughly halfway the main diagonal, which signals $\pi\cdots\pi$ interactions. These are due to extended stacking arrangements of the quinoline rings, which all lie roughly orthogonal to the $[10\bar{1}]$ direction (Figure 2a), along which they form parallel displaced ladders similar to those observed in other quinoline [10,11]

and aromatic compounds [40]. Inversion-related organic moieties are stacked in a perfectly parallel fashion (Supplementary Materials, Section S2), but whenever symmetry-independent rings are close to each other, a slanted arrangement is preferred [40], with quinoline least-squares planes displaying an offset angle of $12.60(2)^\circ$ with respect to each other.

4. Coordination Geometry

The stoichiometry of the CDCQB binuclear complex is $[\text{Cu}(4,7\text{-DCQ})_2\text{Br}_2]_2$, with the metal centers in a formal +2 oxidation state. Inversion-related copper ions are connected through strongly asymmetric $\mu^2\text{-Br}^-$ ligands, resulting in two edge-sharing, distorted square pyramidal units (Figure 3). Each bridging Br(1) atom acts as both an equatorial and axial ligand for the different Cu centers. Similar structures have been reported for Cu complexes with heterocycle aromatics [41–44] or Schiff bases [45–48].

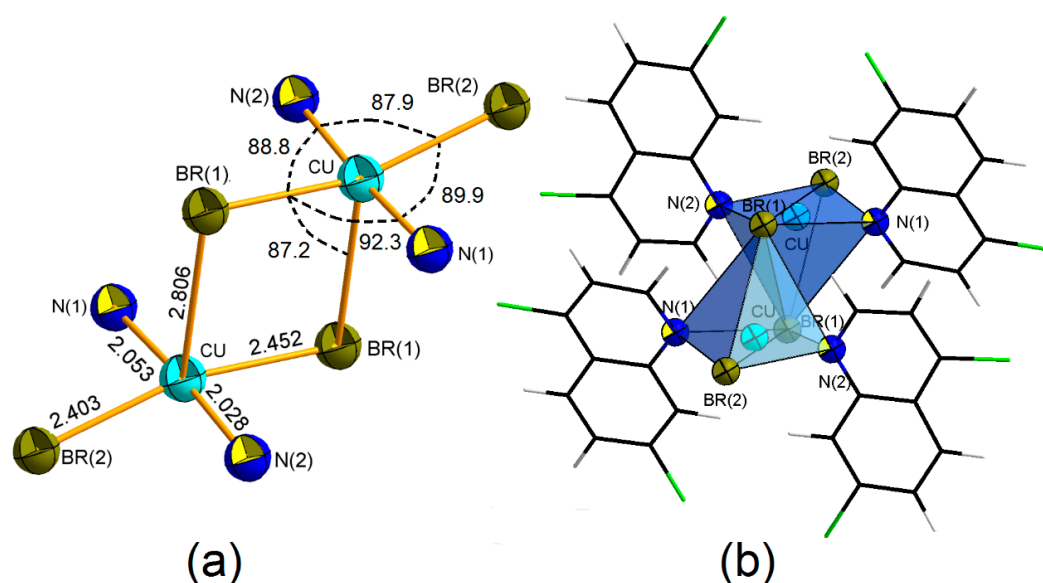


Figure 3. Structure of the binuclear coordination complex CDCQB, as determined by single-crystal X-ray diffraction at $T = 100$ K. Color code is as in Figure 1. Thermal ellipsoids are drawn at the 99% probability level. (a) Geometry of the two inversion-related metal centers. Distances are in Å and angles in degrees. (b) Coordination polyhedra, highlighting the distorted square pyramidal geometry, with respect to the relative orientation of organic ligands. Black lines serve only as guides for the eye.

Equatorial bond distances are within the expected range for organometallic compounds with either pyridine-like (1.998–2.142 Å) or bromide (2.303–2.521 Å) ligands [49]. Distortions in this plane are mainly due to the much larger covalent radius of bromine (1.20(3) Å) with respect to nitrogen (0.71(1) Å) [50]. The metal center is also significantly pyramidalized, as Cu^{2+} ions are displaced by 0.31 Å toward the axial Br(1) ligand (Figure 3a). While the two equatorial Cu–Br interactions bear similar coordination distances, the axial Br(1) bromide is farther from the metal center by ~ 0.35 Å, due to the different nature of the chemical bond in which it is involved (see below). Despite apparent similarities, the coordination geometries of the only other two known $\text{Cu}(\text{II}):4,7\text{-DCQ}$ binuclear complexes (CSD refcodes KUHHEA and KUBJOG [19]) are significantly different, as they both bear k^2 chelating COO^- groups that make copper centers significantly closer to each other (2.7 and 2.8 Å) with respect to CDCQB ($d_{\text{Cu}\cdots\text{Cu}} \cong 3.8$ Å). No direct metal–metal interactions are set up in CDCQB, resulting in much stronger Cu–N coordinative bonds (e.g., $d_{\text{Cu}\cdots\text{N}} \cong 2.16$ Å in KUHHEA and 2.24 Å in KUBJOG).

The crystal field has slight influence on the coordination geometry. Section S3 (Supplementary Materials) reports on in vacuo DFT-optimized geometries, compared with the X-ray one (Figure S11). For the stoichiometric complex, the only relevant change is a $\sim 10.0^\circ$ relative rotation of the quinoline

rings bonded to the same Cu center. This is clearly a packing effect, as in the solid state 4,7-DCQ ligands are constrained by stacking interactions in a more space-saving arrangement (see above and Supplementary Materials, Section S2). However, the Cu local valence shell concentration (VSCC) and depletion coordination geometry are essentially identical, with deviations between bond lengths and angles not exceeding 2% and 3% on average, respectively, regardless of the spin state of the metal (Table S13). In the DFT-optimized structure, the pyramidalization of Cu atoms is less appreciable but still significant, with the metal being displaced by 0.22 Å towards the axial bromide.

5. Chemical Bonding

Local topological descriptors of chemical bonds [22] of CDCQB in the solid state were evaluated to extract qualitative, real-space information on the nature of the coordinative interactions. The purpose is to rank, at least on a relative scale, the relative strength of metal–ligand bonds. Experimental outcomes were compared with those from the multipole-projected charge density, as evaluated by theoretical structure factor amplitudes (F_{theo}) from solid-state DFT M06/pVZT simulations at the same X-ray multipole geometry (Supplementary Materials, Section S1.4). The agreement among experimental and theoretical multipole models is quantitative (Table S16 and Figure S12), indicating that the X-ray charge density is sufficiently accurate to gain reliable insights on the copper first coordination shell.

As expected, the charge density Laplacian, $\nabla^2\rho(\mathbf{r})$, is invariably positive at the bond critical points (bcp's) of the Cu–N and Cu–Br bonds (Table S16), as these interactions fall in the valence shell charge depletion (VSCD) region of the metal [37,51]. No direct metal–metal bonds [52] are detected: the two copper centers are connected through an asymmetric μ -Br bridge that involves Br(1) ions on axial positions (Figure 3). The axial Cu–Br(1) bonds bear a low degree of covalency, with halved $\rho(\mathbf{r})_{\text{bcp}}$ with respect to equatorial Cu–Br bonds.

The Abramov's functional [53] can be exploited to estimate the kinetic energy density at the bcp, $G(\mathbf{r})_{\text{bcp}}$, from the corresponding charge density and its Laplacian, according to the following equation:

$$G(\mathbf{r})_{\text{bcp}} = \frac{3}{10}(3\pi^2)^{2/3} \rho(\mathbf{r})_{\text{bcp}}^{5/3} + \frac{1}{6}\nabla^2\rho(\mathbf{r})_{\text{bcp}} \quad (1)$$

This expression is strictly correct only when the gradient of the charge density is null, such as at a critical point. It relies on the Kirzhnitz-corrected Thomas–Fermi expression for the electron kinetic energy [53], thus being valid only in low-density areas that are far from core electrons, such as the copper valence region of CDCQB (Table S16). The local form of the virial theorem [22] relates kinetic and potential energy densities to the corresponding Laplacian:

$$\frac{\hbar^2}{4m}\nabla^2\rho(\mathbf{r})_{\text{bcp}} = V(\mathbf{r})_{\text{bcp}} + 2G(\mathbf{r})_{\text{bcp}} \quad (2)$$

where $V(\mathbf{r})_{\text{bcp}}$ is the potential energy density, negative for bonded states. The Laplacian of the charge density, together with the total kinetic energy density, $H(\mathbf{r}) = V(\mathbf{r}) + G(\mathbf{r})$, distinguishes electron-shared interaction, characterized by a prevalent contribution of $V(\mathbf{r})$, from the closed-shell (CS) ones, where $G(\mathbf{r})$ dominates. Following Espinosa et al. [54], we compared the bond degree parameter ($\text{BD} = H(\mathbf{r})_{\text{bcp}}/\rho(\mathbf{r})_{\text{bcp}}$) with the $|V(\mathbf{r})|/G(\mathbf{r})$ ratio for all bonds in the valence coordination region of Cu^{2+} , where direct metal–ligand interactions take place.

Experimental estimates are compared with multipole-projected DFT ones in Figure 4 (black squares vs. red triangles). Differences are very small on absolute grounds. Moreover, the least-squares trends of the two series are quantitatively identical, i.e., $\text{BD} = -6.2(4)\cdot|V(\mathbf{r})|/G(\mathbf{r}) + 6.0(4)$ ($R^2 = 0.98$) for F_{exp} and $\text{BD} = -6.0(4)\cdot|V(\mathbf{r})|/G(\mathbf{r}) + 5.8(4)$ ($R^2 = 0.97$) for F_{theo} . The atomic interaction lines whose energy parameters lie in the upper left quadrant of Figure 4 are produced by full closed shell (CS) $\text{Br}\cdots\text{H}$ hydrogen bonds (Figure 2 and Figure S13). Equatorial Cu–Br and Cu–N coordinative bonds fall instead in the lower right region of the diagram, meaning that the nuclear potential is prevailing at their bcp's. Nevertheless, the corresponding Laplacians remain positive as, according to Equation (2),

$G(\mathbf{r}) < V(\mathbf{r}) < 2 \cdot G(\mathbf{r})$. In other words, these bonds fall in a “transit” region, characterized by negative $H(\mathbf{r})$ and positive Laplacian, that is, they experience a certain degree of electron sharing [54,55]. Both theoretical and experimental estimates agree in predicting the Cu–N bonds as more covalent than the Cu–Br ones. On the contrary, the axial $\text{Cu} \cdots \text{Br}(1)$ interaction is instead almost entirely closed-shell, with no appreciable electron sharing ($H(\mathbf{r}) = 0$) or, equivalently, a main electrostatic character. This energy classification can be related only to the relative strength of homologous bonds, as topological descriptors are only indirectly related to attractive Coulomb interactions between formal Cu^{2+} and Br^- ions. The axial $\text{Cu} \cdots \text{Br}(1)$ is certainly weaker than the equatorial Cu–Br ones, as a null electron sharing is accompanied by a significantly greater metal–ligand distance.

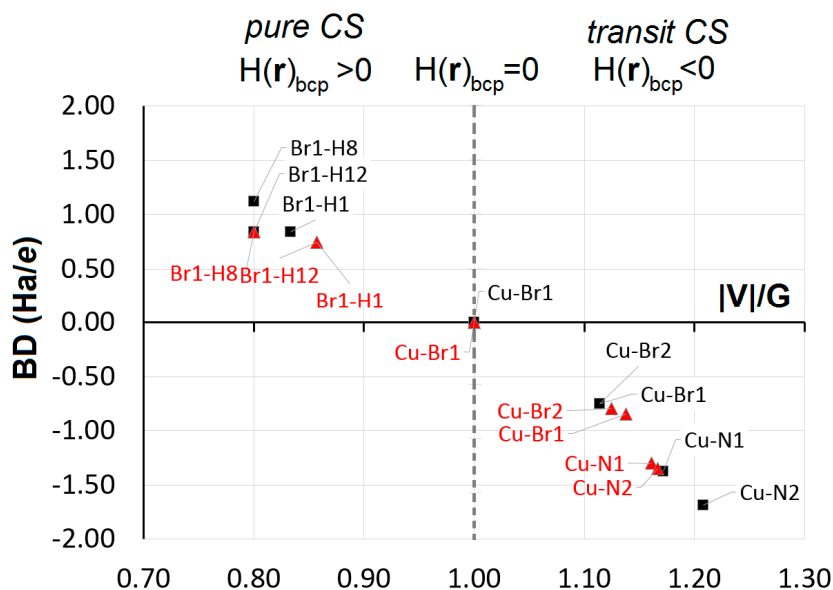


Figure 4. Bond degree parameter ($\text{BD} = H(\mathbf{r})_{\text{bcp}}/\rho(\mathbf{r})_{\text{bcp}}$, atomic units) vs. the adimensional ratio of potential and kinetic energy densities, $|V(\mathbf{r})_{\text{bcp}}|/G(\mathbf{r})_{\text{bcp}}$, for chemical bonds in the valence coordination region of Cu^{2+} . The $|V(\mathbf{r})_{\text{bcp}}|/G(\mathbf{r})_{\text{bcp}} = 1.0$ boundary (dashed grey line) discriminates potential prevailing interactions ($H(\mathbf{r}) < 0$) from kinetic prevailing ones ($H(\mathbf{r}) > 0$). Black squares: experimental results. Red triangles: multipole-projected (F_{theo}) DFT estimates.

The valence shell concentration (VSCC) and depletion zones of the charge density scalar field around Cu^{2+} ions provide hints as to the actual filling of d orbitals. Figure 5 displays the electron density Laplacian along the mutually orthogonal $\text{N}(1)\text{--Cu--N}(2)$ and $\text{Br}(1)\text{--Cu--Br}(2)$ equatorial coordinative bonds. The Laplacian distribution around the metal has a spherical shape. VSCC regions form an almost isotropic belt, according to the relatively low amount of electron sharing experienced by these bonds. If, from the viewpoint of the metal, Cu–Br and Cu–N bonds are qualitatively similar (Figure 5), lone pairs of quinoline N atoms are instead neatly polarized toward the metal, in agreement with the σ -donor character of this interaction.

As d orbitals on Copper are almost filled, we checked whether some kind of π -backdonation occurs, possibly involving antibonding π^* orbitals of the quinoline system. We computed HOMED (Harmonic Oscillator Model of Electron Delocalization) indices [56] of 4,7-DCQ in the experimental and in vacuo DFT-optimized structures, and we compared them with the isolated 4,7-dichloroquinoline ligand (Table 2).

$$\text{HOMED} = 1 - \frac{\alpha}{n} \sum_{i=1}^n (R_0 - R_i)^2 \quad (3)$$

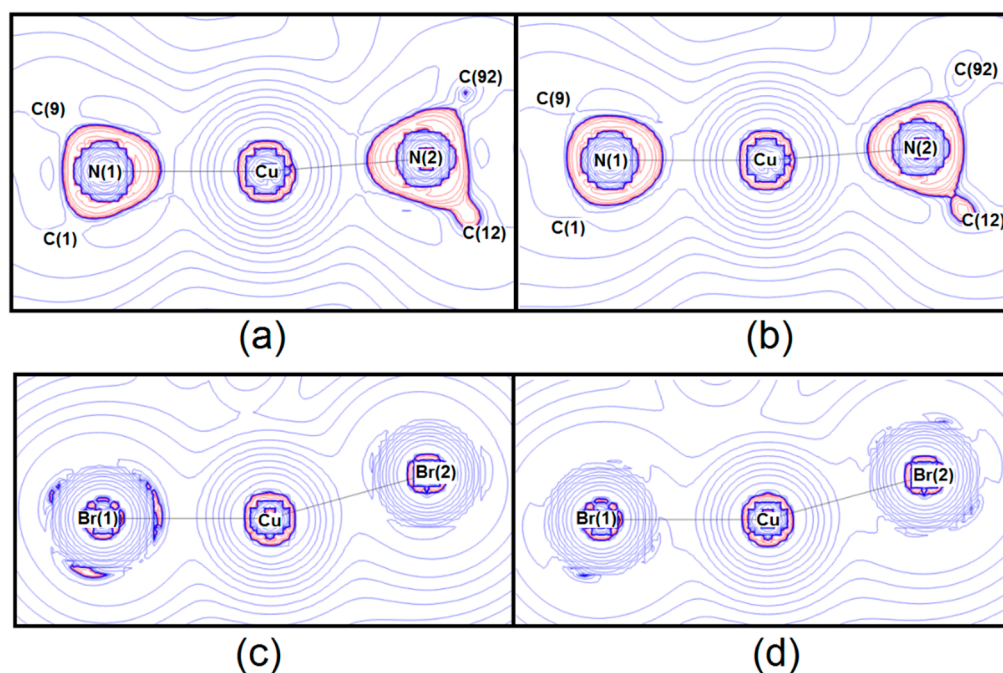


Figure 5. Isocontour maps of $-\nabla^2\rho(\mathbf{r})$ at variable-step ($\pm a \cdot 10^{-n} e/A^5$, with $a = 9.64, 4.82$ and 2.20 and $n = 0, \pm 1, \pm 2, \pm 3, \pm 4$ and ± 5) in planes N(1)–Cu–N(2) (a,b) and Br(1)–Cu–Br(2) (c,d) for equatorial Cu–ligand bonds. Blue lines correspond to regions of charge depletion, while red ones indicate charge concentration. (a,c): Experimental multipole model; (b,d): multipole-projected DFT results (F_{theo}).

Table 2. HOMED indices for aromaticity in symmetry-independent 4,7-dichloroquinoline ligands. Calibration parameters proposed in [56] have been employed ($\alpha(\text{C}=\text{C}) = 88.09 \text{ \AA}^{-2}$; $\alpha(\text{C}=\text{N}) = 91.60 \text{ \AA}^{-2}$; $R_0(\text{C}=\text{C}) = 1.394 \text{ \AA}$; $R_0(\text{C}=\text{N}) = 1.334 \text{ \AA}$). Data in Table S18.

System	X-ray ^a	Isolated Complex, DFT ^b	Isolated Ligand, DFT ^b
Quinoline 1 ^c (total)	0.88	0.87	0.88
Quinoline 2 ^c (total)	0.88	0.88	0.88
Quinoline 1, N-bearing ring ^d	0.87	0.87	0.88
Quinoline 1, C ₆ ring ^e	0.95	0.94	0.94
Quinoline 2, N-bearing ring ^d	0.88	0.89	0.88
Quinoline 2, C ₆ ring ^e	0.96	0.95	0.94

^a Experimental multipole model on single-crystal X-ray diffraction data at 100 K. ^b DFT-optimized structures in the gas phase. Results are independent from the spin state of the metal. See Section 2 for details. ^c See Figure 1 for numbering. Atoms of the “quinoline 2” molecule all have 2-digit ID numbers, ending with “2”. ^d This is the heterocyclic ring and bears the N atom which is connected to copper. ^e All atoms in this ring are carbons.

HOMED relies on the idea that extended electron delocalization should reflect into the equalization of covalent bond lengths, whereas any deviation from an otherwise ideal symmetry implies some loss of aromaticity. R_0 is the reference bond length for a fully delocalized (aromatic) system, R_i is the i -th bond length of each of the n bonds in the ring considered, and α is an empirical calibration parameter chosen so that HOMED is exactly 0 for the Kekulé structure of benzene and is 1 for aromatic benzene [56].

No significant differences are detected when aromaticity indices computed on the experimental structure are compared with those from the isolated complex or ligand. As expected [57], the heterocycle part of the condensed quinoline system is slightly more asymmetric—and thus less aromatic—due to the incorporation of the nitrogen atom. However, Cu–N bonding does not determine any appreciable

effect on the aromatic π system of 4,7-DCQ, ruling out any backdonation from the metal. This result is also in line with the electronic structure analysis (see below).

In conclusion, the chemical bonding analysis demonstrates that each Cu^{2+} ion acts as a Lewis acid, accepting pure σ coordinative bonds from lone pairs of organic nitrogen atoms and Br^- ions, with no appreciable perturbation of π aromatic systems of the 4,7-dichloroquinoline moieties. Axial Br(1) atoms are instead involved in essentially closed-shell interactions, mainly electrostatic in nature and significantly weaker than equatorial Cu–Br ones.

6. Electronic States

The occupational Br(1) defect (see Section 2) implies that a ~11% non-negligible minority of $\text{Cu}_2(4,7\text{-DCQ})_4\text{Br}_3$ moieties with a single bridging Br^- ion coexist with stoichiometric $\text{Cu}_2(4,7\text{-DCQ})_4\text{Br}_4$ ones. To ensure electroneutrality, the bromide vacancy must be compensated by a lower charge on Cu ions. Thus, we expect to have a mixture of +1/+2 oxidation states of copper in the crystal. This view is supported by magnetic susceptibility measurements on the CDCQB complex. An effective magnetic moment $\mu_{\text{eff}} = 2.47$ Bohr magnetons (BM) is reported (Section S5). This estimate is compatible with two unpaired electrons on the two Cu centers and is also consistent with DFT simulations, which predict the triplet spin state as $29.9 \text{ kcal}\cdot\text{mol}^{-1}$ more stable than the singlet one. However, the measured μ_{eff} has a ~12% lower magnitude than that expected for spin-only paramagnetism produced by two unpaired electrons (2.83 BM). In other words, the missing spin polarization can be attributed to the occurrence of an equal amount of Cu centers in a diamagnetic d^{10} configuration. The conformity of views between structural, DFT and magnetic results is remarkable.

Figure 6 displays a simplified molecular orbital (MO) scheme of the neutral asymmetric unit of the CDCQB complex, $\text{Cu}(4,7\text{-DCQ})_2\text{Br}_2$. The geometry is close to a rectangular pyramid, so C_{2v} symmetry labels are used. Only σ -bonding interactions are shown, as they are the most relevant in this system. Moreover, the scheme includes only equatorial ligands, as the axial $\text{Br}(1)^-$ ion does not significantly participate in electron sharing (see above). Moreover, the quinoline system acts as a σ -donor (see above); thus, only the sp^2 hybrids of N atoms directed toward the metal along the y laboratory axis have been included in the calculation of the corresponding symmetry-adapted linear combination (SALC) of atomic orbitals.

The electronic states of ligands, and specifically those of bromide ions, are higher in energy than the metal ones. Therefore, frontier orbitals bear a significant ligand character, at a variance of what is expected in a normal ligand field. For example, the first virtual states bear large contributions from π^* orbitals localized on the quinoline rings, while the highest occupied MO (HOMO) is invariably an antibonding combination of the $d_{x^2-y^2}$ metal state with ligand-centered SALC of a_1 symmetry (see Figure S13). However, the ligand field is not inverted in the Hoffman's sense [8], as the MO sequence is the same as expected for a distorted square pyramidal crystal field (Figure 6). The reason can be traced back to the relatively low electronegativity of ligands. Therefore, frontier orbitals still bear a significant metal character, and the geometry of the title compound can be rationalized in terms of distortions due to an anisotropic ligand environment, according to the predictions of the crystal field theory.

The higher energy of ligand states, however, makes them possible reducing agents with respect to metal. Following Snyder [5], we believe that copper in CDCQB is partly reduced by bromide ligands. Keeping in mind that many arguments arise when one tries to assign physical meaning to quantities sensible to arbitrary partitioning criteria, such as atomic charges, some consistent trends can at least be deduced by comparing the outcomes of DFT simulations. Table 3 shows condensed Mulliken charges of metal, quinoline ligands and bromide ions for the stoichiometric $\text{Cu}_2(4,7\text{-DCQ})_4\text{Br}_4$ structure, at the experimental and in vacuo DFT optimized geometries. DFT results from the triplet spin state are qualitatively identical (Table S21).

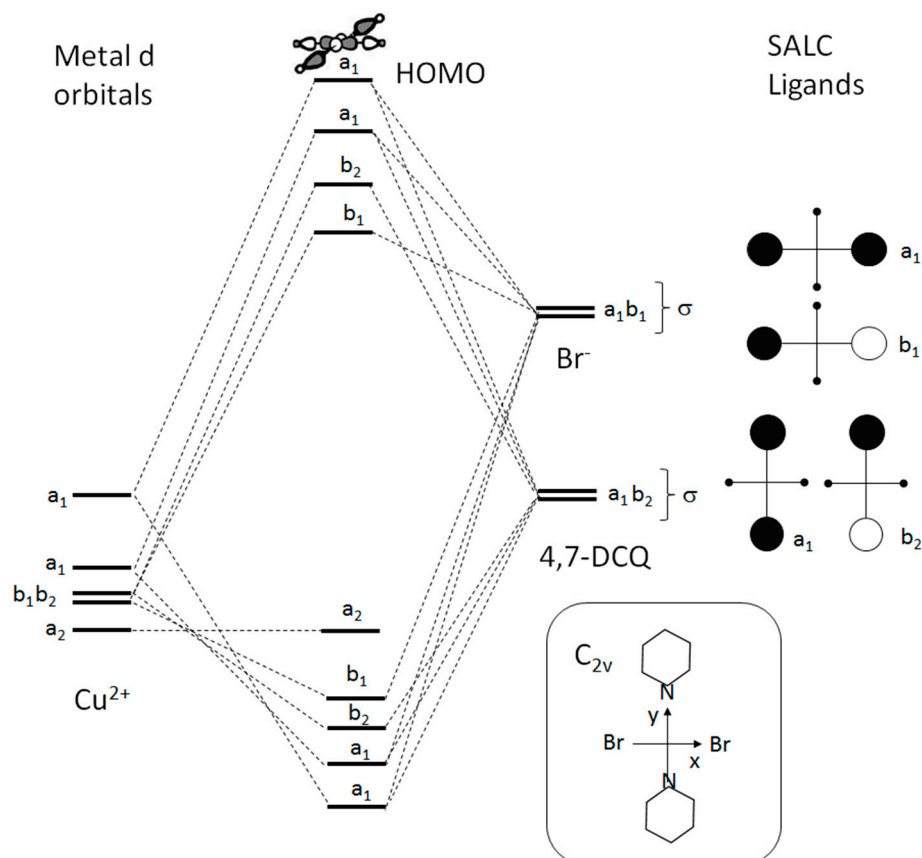


Figure 6. Simplified C_{2v} -idealized valence interaction diagram of each $\text{Cu}(4,7\text{-DCQ})_2\text{Br}_2$ unit in the stoichiometric CDCQB binuclear complex. A d^9 configuration of the Cu^{2+} ion and fully occupied SALC of ligands are assumed.

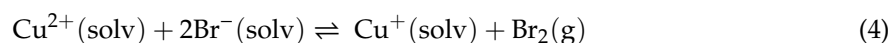
Table 3. Mulliken net atomic charges (electrons) of relevant symmetry-independent chemical moieties in CDCQB, as obtained from M06/TZVP calculations on isolated complexes ^a.

Fragment	X-ray Geometry ^b	DFT-Optimized ^b
$\mu^2\text{-Br}^-$ (Br(1))	-0.781	-0.780
Br^- , equatorial (Br(2))	-0.695	-0.681
Cu	1.298	1.309
4,7-DCQ 1	0.084	0.075
4,7-DCQ 2	0.091	0.075

^a Full data in Table S13 SI. ^b Only the inversion-independent chemical moieties are reported, corresponding to one-half of the full stoichiometry.

While the dichloroquinoline ligands are neutral, some electron density is transferred to copper, whose net charge is lower than that expected from its formal +2 oxidation state. DFT results thus provide a rationale to explain the observed amount of nonstoichiometric $\text{Cu}_2(4,7\text{-DCQ})_4\text{Br}_3$ molecules in the crystal, with reduced (or partially reduced) copper centers (see above).

It is likely that the redox process takes place in solution when CuBr_2 is mixed with the 4,7-DCQ ligand (see Section 2). We hypothesize that a minority of bromide ions are oxidized to Br_2 and produce Cu(I) centers, which are included in the crystal at the growth stage. The reaction is expected to be



where “soln” indicates the 1:1 dichloromethane/methanol reaction liquor (see Section 2). Based on the amount of formal Cu^+ centers found in the crystal, a degree of progress of 11% is reasonable,

corresponding to an equilibrium constant $K = 5.15 \times 10^{-4}$. Overall, the process is endergonic, with $\Delta G^\circ = 18.14 \text{ kJ}\cdot\text{mol}^{-1}$ as computed from the known thermodynamic boundary conditions ($T = 15^\circ\text{C}$, $p = 1 \text{ bar}$; see Section 2). From the Nernst equation, applicable at our dilutions, the expected standard cell potential is -0.188 V for the $\text{Cu}^{2+}/\text{Br}^-$ redox pair. To the sake of comparison, the reduction of Cu^{2+} by bromide in water is much more endergonic, with 5 times higher ΔG° ($+89.6 \text{ kJ}\cdot\text{mol}^{-1}$), as estimated from standard reduction potentials. However, in aqueous solution, Cu(I) is completely unstable and disproportionates to give metallic copper and Cu(II) ions. Copper(I) oxidation state can be stabilized only by forming stable complexes (e.g., $[\text{CuCl}_2]^-$) or insoluble salts (e.g., CuI).

The difference between the two ΔG° values can be partly attributed to the different chemical environments [58,59], although the role of 4,7-DCQ may not be negligible. Indeed, it is known that the Cu(I)–Cu(II) redox system can be strongly influenced by the presence of N-donor ligand depending on the strength of the copper–nitrogen bond [60]. Actually, stabilization effects towards an oxidation state in a copper complex are governed by a tricky combination of structural and reduction–oxidation properties of both organic components and Cu counter-anions [61,62]. Even some environmental factors, such as temperature and solvent polarity, can also produce a drastic change in the position of the redox equilibrium [63]. To corroborate this model and fully clarify the role of any system elements, the inclusion of further experimental evidence is needed, which will be discussed in a forthcoming study.

7. Conclusions

The stereochemistry of Cu^{2+} complexes is often determined by a subtle interplay of electronic effects that are hardly rationalized in a classical coordination chemistry framework. In this work, the binuclear $[\text{Cu}(4,7\text{-dichloroquinoline})_2\text{Br}_2]_2$ complex (CDCQB) was studied by single-crystal X-ray crystallography and quantum chemical methods as a possible borderline case between transition and main group chemistry. The basic coordination geometry of CDCQB is distorted square pyramidal, with each Cu center bonded to four equatorial ligands and one axial bridging bromide ion. There are striking similarities with inverted field complexes. However, likely due to the low electronegativity of 4,7-DCQ and bromide, the MO sequence remains that expected for a distorted square pyramidal crystal field, that is, no inversion of the d ladder occurs.

From the reactivity viewpoint, we provided several points of experimental evidence that formal Cu^{2+} centers in this complex act as Lewis acids and tend to accept electrons from the inner shell ligands, in agreement with the known reactivity and catalytic ability of this kind of complex [17,18,64]. To date, only two crystal structures of Cu(II):4,7-dichloroquinoline complexes have been reported (CSD refcodes KUBJOG and KUHHEA), and a few dozen Cu:quinoline complexes are known, with copper mainly in the +1 oxidation state. We proved that 4,7-DCQ ligands, in conjunction with bromide counterions, can promote a change of the metal redox state. In further detail, it is found that $\sim 11\%$ Br^- vacancies are included in the crystal, determining defective $\text{Cu}_2(4,7\text{-DCQ})_4\text{Br}_3$ binuclear units, with a missing μ^2 -type bromide ion, that coexist with stoichiometric $\text{Cu}_2(4,7\text{-DCQ})_4\text{Br}_4$ ones. To ensure electroneutrality, copper in $\text{Cu}_2(4,7\text{-DCQ})_4\text{Br}_3$ must thus be partially reduced. An endergonic redox pair where Br_2 is produced by the partial oxidation of Br^- is probably set up in solution, and the resulting Cu(I) centers are included in the crystal during the growth process. Even though no appreciable π -backdonation toward the 4,7-DCQ moieties was detected, we note that the availability of low-energy virtual π^* 4,7-DCQ orbitals may provide opportunities to activate the aromatic ring of the ligand, opening new perspectives for aromatic chemistry applications.

Supplementary Materials: The following are available online at <http://www.mdpi.com/2073-4352/10/6/477/s1>. Structure factor amplitudes at 100 K. Multipole model output. Details on the development of the final multipole model. Handling of disorder and anharmonicity. Strategy of the multipole refinement. Bulk quantum simulations and multipole-projected charge densities. Least-squares results. Crystal packing: nature of halogen–halogen contacts. Stacking motifs. Geometry: relative ligand orientation and DFT-optimized coordinates. Charge density and aromaticity descriptors. Magnetic susceptibility measurements. Frontier molecular orbitals. Figure S1: X-ray quality crystal. Figures S2 and S3: Anharmonicity. Figure S4: Normal Probability Plot. Figures S5 and S6: Fourier residuals. Figures S7 and S8: halogen bonded motifs. Figures S9 and S10: Stacking motifs. Figure S11:

DFT-optimized geometries. Figure S12: Topological molecular graph. Figure S13: Frontier orbitals. Table S1: Least-squares results. Table 1: Agreement factors. Coordinates and Uiso at 100 K. Table S3: Harmonic ADP's. Table S4: Anharmonic Graham-Charlier coefficients. Tables S5-S9: Multipole coefficients. Table S10: Halogen...hydrogen contacts. Table S11: Halogen-bonded interactions. Table S12: Stacking distances. Table S13: Coordination geometries. Tables S14 and S15: DFT-optimized coordinates. Tables S16 and S17: Relevant bcp properties. Table S18: Bond lengths in aromatic rings. Table S19: Magnetic data. Table S20: Pascal shielding constants. Table S21: Mulliken charges.

Author Contributions: Conceptualization, S.R. and L.L.P.; Data curation, G.F.; Formal analysis, G.F. and G.M.; Investigation, G.F., S.R., G.M. and G.T.; Supervision, L.L.P.; Writing—original draft, L.L.P.; Writing—review & editing, S.R., G.M. and L.L.P. All authors have read and agreed to the published version of the manuscript.

Funding: This research received no external funding.

Acknowledgments: The supercomputing center CINECA is warmly acknowledge for provision of computational resources through ISCRA C grants HP10C4QH2 and HPL13PXLVY.

Conflicts of Interest: The authors declare no conflict of interest.

References

1. Reinen, D. Cu^{2+} , a Chameleon in Coordination Chemistry. *Comments Inorg. Chem.* **1983**, *2*, 227–246. [[CrossRef](#)]
2. Persson, I.; Persson, P.; Sandström, M.; Ullström, A.-S. Structure of Jahn–Teller distorted solvated copper(ii) ions in solution, and in solids with apparently regular octahedral coordination geometry. *J. Chem. Soc. Dalton Trans.* **2002**, *7*, 1256–1265. [[CrossRef](#)]
3. Chaboy, J.; Muñoz-Páez, A.; Merklings, P.J.; Sánchez Marcos, E. The hydration of Cu^{2+} : Can the Jahn-Teller effect be detected in liquid solution? *J. Chem. Phys.* **2006**, *124*, 064509. [[CrossRef](#)] [[PubMed](#)]
4. Rodríguez, F. Unveiling the Local Structure of Cu^{2+} Ions from d-Orbital Splitting. Application to K_2ZnF_4 : Cu^{2+} and KZnF_3 : Cu^{2+} . *Inorg. Chem.* **2017**, *56*, 2029–2036. [[CrossRef](#)] [[PubMed](#)]
5. Snyder, J.P. Elusiveness of Cu(III) Complexation; Preference for Trifluoromethyl Oxidation in the Formation of $[\text{Cu}(\text{CF}_3)_4]^-$ Salts. *Angew. Chem. Int. Ed. Engl.* **1995**, *34*, 80–81. [[CrossRef](#)]
6. Aullón, G.; Alvarez, S. Oxidation states, atomic charges and orbital populations in transition metal complexes. *Theor. Chem. Acc.* **2009**, *123*, 67–73. [[CrossRef](#)]
7. Walroth, R.C.; Lukens, J.T.; MacMillan, S.N.; Finkelstein, K.D.; Lancaster, K.M. Spectroscopic Evidence for a 3d 10 Ground State Electronic Configuration and Ligand Field Inversion in $[\text{Cu}(\text{CF}_3)_4]^{1-}$. *J. Am. Chem. Soc.* **2016**, *138*, 1922–1931. [[CrossRef](#)]
8. Hoffmann, R.; Alvarez, S.; Mealli, C.; Falceto, A.; Cahill, T.J.; Zeng, T.; Manca, G. From Widely Accepted Concepts in Coordination Chemistry to Inverted Ligand Fields. *Chem. Rev.* **2016**, *116*, 8173–8192. [[CrossRef](#)]
9. Macetti, G.; Rizzato, S.; Beghi, F.; Silvestrini, L.; Presti, L. Lo On the molecular basis of the activity of the antimalarial drug chloroquine: EXAFS-assisted DFT evidence of a direct Fe–N bond with free heme in solution. *Phys. Scr.* **2016**, *91*, 023001. [[CrossRef](#)]
10. Macetti, G.; Loconte, L.; Rizzato, S.; Gatti, C.; Lo Presti, L. Intermolecular Recognition of the Antimalarial Drug Chloroquine: A Quantum Theory of Atoms in Molecules–Density Functional Theory Investigation of the Hydrated Dihydrogen Phosphate Salt from the 103 K X-ray Structure. *Cryst. Growth Des.* **2016**, *16*, 6043–6054. [[CrossRef](#)]
11. Sacchi, P.; Loconte, L.; Macetti, G.; Rizzato, S.; Lo Presti, L. Correlations of Crystal Structure and Solubility in Organic Salts: The Case of the Antiplasmodial Drug Piperaquine. *Cryst. Growth Des.* **2019**, *19*, 1399–1410. [[CrossRef](#)]
12. Costello, L.C.; Franklin, R.B. A comprehensive review of the role of zinc in normal prostate function and metabolism; and its implications in prostate cancer. *Arch. Biochem. Biophys.* **2016**, *611*, 100–112. [[CrossRef](#)]
13. Di Vaira, M.; Bazzicalupi, C.; Orioli, P.; Messori, L.; Bruni, B.; Zatta, P. Cloroquinol, a Drug for Alzheimer's Disease Specifically Interfering with Brain Metal Metabolism: Structural Characterization of Its Zinc(II) and Copper(II) Complexes. *Inorg. Chem.* **2004**, *43*, 3795–3797. [[CrossRef](#)] [[PubMed](#)]
14. Zanon, V.S.; Lima, J.A.; Cuya, T.; Lima, F.R.S.; da Fonseca, A.C.C.; Gomez, J.G.; Ribeiro, R.R.; França, T.C.C.; Vargas, M.D. In-vitro evaluation studies of 7-chloro-4-aminoquinoline Schiff bases and their copper complexes as cholinesterase inhibitors. *J. Inorg. Biochem.* **2019**, *191*, 183–193. [[CrossRef](#)] [[PubMed](#)]

15. Birks, J.S. Cholinesterase inhibitors for Alzheimer's disease. In *Cochrane Database of Systematic Reviews*; Birks, J.S., Ed.; John Wiley & Sons, Ltd.: Chichester, UK, 2006.
16. Touret, F.; de Lamballerie, X. Of chloroquine and COVID-19. *Antivir. Res.* **2020**, *177*, 104762. [[CrossRef](#)]
17. Cohen, T.; Schambach, R.A. The Copper–Quinoline Decarboxylation. *J. Am. Chem. Soc.* **1970**, *92*, 3189–3190. [[CrossRef](#)]
18. Cahiez, G.; Moyeux, A.; Gager, O.; Poizat, M. Copper-Catalyzed Decarboxylation of Aromatic Carboxylic Acids: En Route to Milder Reaction Conditions. *Adv. Synth. Catal.* **2013**, *355*, 790–796. [[CrossRef](#)]
19. Kawata, T.; Uekusa, H.; Ohba, S.; Furukawa, T.; Tokii, T.; Muto, Y.; Kato, M. Magneto-structural correlation in dimeric copper(II) benzoates. *Acta Crystallogr. Sect. B* **1992**, *48*, 253–261. [[CrossRef](#)]
20. Hiller, W. The Crystal Structure of [(Quinoline)₂CuI]₂, CH₃CN. *Z. Naturforsch.* **1984**, *39b*, 861–863. [[CrossRef](#)]
21. Engelhardt, L.M.; Healy, P.C.; Kildea, J.D.; White, A.H. Lewis-base adducts of group 11 metal(i) compounds. LIII: Synthesis and structural characterization of binuclear μ , μ' -dichloro-, dibromo- and diiodo-bis(pyridine)(triphenylphosphine)copper(i) complexes, and their pyridine-4-carbonitrile analogues. *Aust. J. Chem.* **1989**, *42*, 913–922. [[CrossRef](#)]
22. Bader, R.F.W. *Atoms in Molecules: A Quantum Theory, International Series of Monographs on Chemistry 22*; Clarendon Press: Oxford, UK, 1990; ISBN 9780198558651.
23. Madsen, A.Ø. SHADE web server for estimation of hydrogen anisotropic displacement parameters. *J. Appl. Crystallogr.* **2006**, *39*, 757–758. [[CrossRef](#)]
24. Bruker AXS Inc. *APEX II SAINT and SADABS User Manuals*; Bruker AXS Inc.: Madison, WI, USA, 2014.
25. Sheldrick, G.M. Crystal structure refinement with SHELXL. *Acta Crystallogr. Sect. C Struct. Chem.* **2015**, *71*, 3–8. [[CrossRef](#)] [[PubMed](#)]
26. Bain, G.A.; Berry, J.F. Diamagnetic Corrections and Pascal's Constants. *J. Chem. Educ.* **2008**, *85*, 532. [[CrossRef](#)]
27. Frisch, M.J.; Trucks, G.W.; Schlegel, H.B.; Scuseria, G.E.; Robb, M.A.; Cheeseman, J.R.; Scalmani, G.; Barone, V. *Gaussian 09, Revis. D.01*; Gaussian Inc.: Wallingford, UK, 2009.
28. Zhao, Y.; Truhlar, D.G. The M06 suite of density functionals for main group thermochemistry, thermochemical kinetics, noncovalent interactions, excited states, and transition elements: Two new functionals and systematic testing of four M06-class functionals and 12 other function. *Theor. Chem. Acc.* **2008**, *120*, 215–241. [[CrossRef](#)]
29. Gionda, A.; Macetti, G.; Loconte, L.; Rizzato, S.; Orlando, A.M.; Gatti, C.; Lo Presti, L. A variable-temperature X-ray diffraction and theoretical study of conformational polymorphism in a complex organic molecule (DTC). *RSC Adv.* **2018**, *8*, 38445–38454. [[CrossRef](#)]
30. Peintinger, M.F.; Oliveira, D.V.; Bredow, T. Consistent Gaussian basis sets of triple-zeta valence with polarization quality for solid-state calculations. *J. Comput. Chem.* **2013**, *34*, 451–459. [[CrossRef](#)]
31. Allen, F.H.; Bruno, I.J. Bond lengths in organic and metal-organic compounds revisited: X–H bond lengths from neutron diffraction data. *Acta Crystallogr. Sect. B Struct. Sci.* **2010**, *66*, 380–386. [[CrossRef](#)]
32. Roversi, P.; Destro, R. Approximate anisotropic displacement parameters for H atoms in molecular crystals. *Chem. Phys. Lett.* **2004**, *386*, 472–478. [[CrossRef](#)]
33. Hansen, N.K.; Coppens, P. Testing aspherical atom refinements on small-molecule data sets. *Acta Crystallogr. Sect. A* **1978**, *34*, 909–921. [[CrossRef](#)]
34. Koritsanszky, T.; Mallinson, P.R.; Macchi, P.; Volkov, A.; Gatti, C.; Richter, T.; Farrugia, L.J. XD2006-A Computer Program Package for Multipole Refinement, Topological Analysis of Charge Densities and Evaluation of Intermolecular Energies from Experimental and Theoretical Structure Factors. In *Users' Manual*; University at Buffalo: Buffalo, NY, USA, 2006.
35. Su, Z.; Coppens, P. Nonlinear Least-Squares Fitting of Numerical Relativistic Atomic Wave Functions by a Linear Combination of Slater-Type Functions for Atoms with $Z = 1$ –36. *Acta Crystallogr. Sect. A Found. Crystallogr.* **1998**, *54*, 646–652. [[CrossRef](#)]
36. Lo Presti, L.; Sist, M.; Loconte, L.; Pinto, A.; Tamborini, L.; Gatti, C. Rationalizing the lacking of inversion symmetry in a noncentrosymmetric polar racemate: An experimental and theoretical study. *Cryst. Growth Des.* **2014**, *14*, 5822–5833. [[CrossRef](#)]
37. Destro, R.; Ruffo, R.; Roversi, P.; Soave, R.; Loconte, L.; Lo Presti, L. Anharmonic motions versus dynamic disorder at the Mg ion from the charge densities in pyrope (Mg₃Al₂Si₃O₁₂) crystals at 30 K: Six of one, half a dozen of the other. *Acta Crystallogr. Sect. B Struct. Sci. Cryst. Eng. Mater.* **2017**, *73*, 722–736. [[CrossRef](#)] [[PubMed](#)]

38. Lo Presti, L. On the significance of weak hydrogen bonds in crystal packing: A large databank comparison of polymorphic structures. *CrystEngComm* **2018**, *20*, 5976–5989. [[CrossRef](#)]
39. Destro, R.; Sartirana, E.; Loconte, L.; Soave, R.; Colombo, P.; Destro, C.; Lo Presti, L. Competing C=O...C=O, C-H...O, Cl...O, and Cl...Cl interactions governing the structural phase transition of 2,6-dichloro-p-benzoquinone at $T_c = 122.6$ K. *Cryst. Growth Des.* **2013**, *13*, 4571–4582. [[CrossRef](#)]
40. Colombo, V.; Lo Presti, L.; Gavezzotti, A. Two-component organic crystals without hydrogen bonding: Structure and intermolecular interactions in bimolecular stacking. *CrystEngComm* **2017**, *19*, 2413–2423. [[CrossRef](#)]
41. Zhao, J.P.; Xie, Y.; Li, J.R.; Bu, X.H. Structural and magnetic modulations of copper(II) azido complexes: Unexpected in situ reactions of mono-N-donor pyridine-based co-ligands. *Dalton Trans.* **2016**, *45*, 1514–1524. [[CrossRef](#)]
42. Villa-Pérez, C.; Cadavid-Vargas, J.F.; Di Virgilio, A.L.; Echeverría, G.A.; Camí, G.E.; Soria, D.B. Crystal structure, Hirshfeld surface analysis, spectroscopic and biological studies on sulfamethazine and sulfaquinoxaline ternary complexes with 2,2'-biquinoline. *New J. Chem.* **2018**, *42*, 891–901. [[CrossRef](#)]
43. Viossat, B.; Gaucher, J.F.; Mazurier, A.; Selkti, M.; Tomas, A. Crystals structure of bis(μ -chloro)bis[chloro-(o-phenanthroline-N,N')-copper(II)], $\text{Cu}_2(\text{C}_{12}\text{H}_8\text{N}_2)_2(\text{Cl}_2)_2$. *Z. Krist. New Cryst. Struct.* **1998**, *213*, 21–23. [[CrossRef](#)]
44. Rösener, T.; Hoffmann, A.; Herres-Pawlis, S. Next Generation of Guanidine Quinoline Copper Complexes for Highly Controlled ATRP: Influence of Backbone Substitution on Redox Chemistry and Solubility. *Eur. J. Inorg. Chem.* **2018**, *2018*, 3164–3175. [[CrossRef](#)]
45. Clark, G.R.; Waters, J.M.; Waters, T.N.; Williams, G.J. Polymorphism in Schiff base complexes of copper(II): The crystal and molecular structure of a second brown form of bis(N-methyl-2-hydroxy-1-naphthaldiminato)copper(II). *J. Inorg. Nucl. Chem.* **1977**, *39*, 1971–1975. [[CrossRef](#)]
46. Creaven, B.S.; Devereux, M.; Karcz, D.; Kellett, A.; McCann, M.; Noble, A.; Walsh, M. Copper(II) complexes of coumarin-derived Schiff bases and their anti-Candida activity. *J. Inorg. Biochem.* **2009**, *103*, 1196–1203. [[CrossRef](#)] [[PubMed](#)]
47. Sydoruk, T.V.; Buvaylo, E.A.; Kokozyay, V.N.; Vassilyeva, O.Y.; Skelton, B.W. Bis(μ -2-methoxy-6-[(methylimino)methyl]phenolato)bis([2-methoxy-6-[(methylimino)methyl]phenolato)copper(II)). *Acta Crystallogr. Sect. E Struct. Reports Online* **2013**, *69*, m551–m552. [[CrossRef](#)] [[PubMed](#)]
48. Sang, Y.L.; Lin, X.S. Synthesis and crystal structures of two Schiff base copper(II) complexes derived from 4-chloro-2-[(2-morpholin-4-ylethylimino)methyl]phenol. *Russ. J. Coord. Chem.* **2010**, *36*, 472–476. [[CrossRef](#)]
49. Orpen, A.G.; Brammer, L.; Allen, F.H.; Kennard, O.; Watson, D.G.; Taylor, R. Supplement. Tables of bond lengths determined by X-ray and neutron diffraction. Part 2. Organometallic compounds and co-ordination complexes of the d- and f-block metals. *J. Chem. Soc. Dalton Trans.* **1989**, *12*, S1–S83. [[CrossRef](#)]
50. Cordero, B.; Gómez, V.; Platero-Prats, A.E.; Revés, M.; Echeverría, J.; Cremades, E.; Barragán, F.; Alvarez, S. Covalent radii revisited. *J. Chem. Soc. Dalton Trans.* **2008**, *21*, 2832–2838. [[CrossRef](#)] [[PubMed](#)]
51. Lo Presti, L.; Destro, R. Experimental and theoretical charge density distribution of the colossal magnetoresistive transition metal sulfide FeCr_2S_4 . *J. Chem. Phys.* **2008**, *128*, 044710. [[CrossRef](#)] [[PubMed](#)]
52. Bianchi, R.; Gervasio, G.; Marabello, D. Experimental electron density in the triclinic phase of $\text{Co}_2(\text{CO})_6(\mu\text{-CO})(\mu\text{-C}_4\text{O}_2\text{H}_2)$ at 120 K. *Acta Crystallogr. Sect. B Struct. Sci.* **2001**, *57*, 638–645. [[CrossRef](#)]
53. Abramov, Y.A. On the Possibility of Kinetic Energy Density Evaluation from the Experimental Electron-Density Distribution. *Acta Crystallogr. Sect. A Found. Crystallogr.* **1997**, *53*, 264–272. [[CrossRef](#)]
54. Espinosa, E.; Alkorta, I.; Elguero, J.; Molins, E. From weak to strong interactions: A comprehensive analysis of the topological and energetic properties of the electron density distribution involving X-H...F-Y systems. *J. Chem. Phys.* **2002**, *117*, 5529–5542. [[CrossRef](#)]
55. Bianchi, R.; Gervasio, G.; Marabello, D. The experimental charge density in transition metal compounds. *C R. Chim.* **2005**, *8*, 1392–1399. [[CrossRef](#)]
56. Raczyńska, E.D.; Hallman, M.; Kolczyńska, K.; Stepniewski, T.M. On the Harmonic Oscillator Model of Electron Delocalization (HOMED) index and its application to heteroatomic π -electron systems. *Symmetry* **2010**, *2*, 1485–1509. [[CrossRef](#)]
57. Gatti, C.; Orlando, A.M.; Monza, E.; Lo Presti, L. Exploring Chemistry Through the Source Function for the Electron and the Electron Spin Densities. In *Applications of Topological Methods in Molecular Chemistry*; Chauvin, R., Lepetit, C., Silvi, B., Alikhani, E., Eds.; Springer: Cham, Switzerland, 2016; pp. 101–129.

58. Tariq, M. Electrochemistry of Br-/Br₂ Redox Couple in Acetonitrile, Methanol and Mix Media of Acetonitrile-Methanol: An Insight into Redox Behavior of Bromide on Platinum (Pt) and Gold (Au) Electrode. *Z. Phys. Chem.* **2020**, *234*, 295–312. [[CrossRef](#)]
59. Desmarquest, J.P.; Trinh-Dinh, C.; Bloch, O. Determination electrochimique des potentiels normaux des couples oxydo-reducteurs Cu²⁺/Cu⁺ et Cu⁺/Cu⁰ dans le methanol. *J. Electroanal. Chem.* **1970**, *27*, 101–108. [[CrossRef](#)]
60. Goodname, D.M.L.; Goodname, M.; Canham, G.W.R. Reversible Oxidation of Copper(I) Iodide in the Presence of Imidazole. *Nature* **1969**, *222*, 866.
61. Banthia, S.; Samanta, A. In Situ Reduction of Copper(II) Forming an Unusually Air Stable Linear Complex of Copper(I) with a Fluorescent Tag. *Inorg. Chem.* **2004**, *43*, 6890–6892. [[CrossRef](#)] [[PubMed](#)]
62. Ziesak, A.; Wesp, T.; Hübner, O.; Kaifer, E.; Wadepohl, H.; Himmel, H.-J. Counter-ligand control of the electronic structure in dinuclear copper-tetrakisguanidine complexes. *Dalton Trans.* **2015**, *44*, 19111–19125. [[CrossRef](#)]
63. Ukpong, E.J.; Akpanudo, N.W.; Prasad, J. Redox and spectral behaviour of copper (II)-chloro and bromo complexes in some nonaqueous solvents. *Afr. J. Pure Appl. Chem.* **2010**, *4*, 38–43.
64. Evans, D.A.; Burgey, C.S.; Kozlowski, M.C.; Tregay, S.W. C₂-Symmetric Copper(II) Complexes as Chiral Lewis Acids. Scope and Mechanism of the Catalytic Enantioselective Aldol Additions of Enolsilanes to Pyruvate Esters. *J. Am. Chem. Soc.* **1999**, *121*, 686–699. [[CrossRef](#)]



© 2020 by the authors. Licensee MDPI, Basel, Switzerland. This article is an open access article distributed under the terms and conditions of the Creative Commons Attribution (CC BY) license (<http://creativecommons.org/licenses/by/4.0/>).